The differences between storms driven by helmet streamer CIRs and storms driven by pseudostreamer CIRs

Joseph E. Borovsky[1,2,3] and Michael H. Denton[1,2]

Received 8 September 2012; revised 30 July 2013; accepted 18 August 2013; published 6 September 2013.

[1] A corotating interaction region (CIR) is formed when fast coronal hole origin solar wind overtakes slow solar wind and forms a region of compressed plasma and magnetic field. The slow wind upstream of the coronal hole fast wind can be either of helmet streamer origin or pseudostreamer origin. For a collection of 125 CIR-driven geomagnetic storms, the slow wind ahead of each CIR is examined; for those storm not containing ejecta, each CIR is categorized as a helmet streamer CIR (74 of the 125 storms) or a pseudostreamer CIR (11 of the 125 storms). Separate superposed epoch studies are performed on the two groups to discern the differences between storms driven by pseudostreamer CIRs and those driven by helmet streamer CIRs. A major difference is that pseudostreamer CIR storms tend not to have a calm before the storm, so the outer plasmasphere does not refill before storm onset, and the outer electron radiation belt does not exhibit a pre-storm decay. The superdense plasma sheet is weaker for pseudostreamer CIR storms, and the dropout of the electron radiation belt is weaker. Pseudostreamer CIR storms and helmet streamer CIR storms tend to be of the same strength as measured by the magnitude of *Kp*, MBI (midnight boundary index), or *Dst*.

Citation: Borovsky, J. E., and M. H. Denton (2013), The differences between storms driven by helmet streamer CIRs and storms driven by pseudostreamer CIRs, *J. Geophys. Res. Space Physics*, *118*, 5506–5521, doi:10.1002/jgra.50524.

1. Introduction

[2] There are two major types of drivers of geomagnetic storms: (1) coronal mass ejections (CMEs) and the sheaths that precede them and (2) corotating interaction regions (CIRs) and the high-speed streams that follow them. These two drivers produce storms with different phenomenologies; hence, it is convenient to divide storms into two types: CME-driven storms and CIR-driven storms [*Borovsky and Denton*, 2006; *Denton et al*., 2006]. CME-driven storms are of particular interest for their strong ring current perturbations, for their geomagnetically induced ground currents, for the possibility of producing new inner radiation belts, and for their associations with solar flare disturbances of the ionosphere and with solar energetic particle events. Other phenomena associated with CME-driven storms are storm sudden commencements, polar cap potential saturation, and global sawtooth oscillations [*Borovsky and Denton*, 2006]. CIR-driven storms are of particular interest for the high fluxes of relativistic electrons produced in the outer radiation belt and for the high levels of spacecraft charging. Other phenomena associated with CIR-driven storms are calms before the storms and long-duration plasmaspheric drainage plumes. CIR-driven storms tend to repeat on a 27 day cycle; CME-driven storms do not.

[3] CME-driven storms can be categorized as to whether the storm is driven by the sheath (with a strong compressed Parker spiral magnetic field) or by the magnetic cloud of the CME (with a strong non-Parker spiral magnetic field), or by both.

[4] We argue here that CIR-driven storms should also be divided into two types: storms driven by helmet streamer CIRs and storms driven by pseudostreamer CIRs. The two types will be shown to have systematically different phenomenologies (cf. Table 1).

[5] A corotating interaction region is formed by fast wind overtaking slow wind, producing an oblique interaction region wherein the slow and fast plasmas are compressed. When a CIR passes the Earth, chronologically, the Earth experiences slow wind before the CIR, then the compressed slow wind of the CIR, then the passage of the CIR stream interface, then the compressed fast wind of the CIR, then an interval of fast wind (a high-speed stream) [cf. *Richardson et al*., 1996, Figure 1; *Borovsky and Denton*, 2009a, Table 1, Figure 2]. Associated with the slow wind prior to the CIR, the Earth may experience a "calm before the storm" with anomalously low geomagnetic activity [*Borovsky and Steinberg*, 2006]: the calm is associated with a buildup of the outer plasmasphere [*Denton and Borovsky*, 2008], a temporal decay of the outer electron radiation belt [*Borovsky and Denton*, 2009a], and the preconditioning of the magnetosphere for the ensuing storm [*Borovsky and Steinberg*, 2006]. Some of the phenomenology of the storm is driven by the compressed solar wind plasma of the CIR: the superdense

[1]Space Science Institute, Boulder, Colorado, USA.
[2]Lancaster University, Lancaster, UK.
[3]University of Michigan, Ann Arbor, Michigan, USA.

Corresponding author: J. E. Borovsky, Space Science Institute, 4750 Walnut, Suite 205, Boulder, CO 80301, USA. (jborovsky@spacescience.org)

2169-9380/13/10.1002/jgra.50524

Table 1. The Similarities and Differences Between Helmet Streamer CIR-Driven Storms and Pseudostreamer CIR-Driven Storms

	Storm Feature	Helmet Streamer CIRs	Pseudostreamer CIRs
	Solar Wind		
1	IMF sector reversal	Yes	No
2	Speed of pre-storm slow wind	Slower	Not as slow
3	Duration of high-speed stream	Longer	Shorter
4	Compression of magnetic field	Strong	Strong
5	Number density at storm onset	High	Normal
6	Ram pressure at storm onset	Very high	High
7	Alfven Mach number during storm	Not as high	High
	Magnetospheric Activity		
8	Calm before the storm	Yes	No
9	Storm strength (*Kp*, PCI)	Strong	Strong
10	*Dst* perturbation of storm	Similar	Similar
	Plasmasphere		
11	Pre-storm refilling of outer plasmasphere	Yes	No
12	Strong drainage plumes	Yes	Yes
	Plasma Sheet		
13	Superdense plasma sheet	Strong	Not as strong
14	Extra hot plasma sheet	Yes	Yes
15	High levels of spacecraft charging	Yes	Yes
	Geomagnetic Field at Geosynchronous Orbit		
16	Strong compression of dayside field	Yes	No
17	Extreme nightside stretching	Yes	Yes
18	Storm time amplitude of ULF fluctuations	High	High
	Outer Electron Radiation Belt		
19	Pre-storm decay of radiation belt	Yes	Possibly no
20	Radiation belt dropout	Yes	Weaker
21	Storm time heating	Yes	Yes
22	Relativistic flux intensification	Yes	Yes

plasma sheet [*Denton and Borovsky*, 2009], the radiation belt dropout [*Borovsky and Denton*, 2009a], and the extreme stretching of the nightside magnetic field [*Borovsky and Denton*, 2010b]. Other phenomena of the storm are driven by the fast solar wind following the CIR: the long-duration plasmaspheric drainage plumes [*Borovsky and Denton*, 2008], the heating of the outer electron radiation belt [*Borovsky and Denton*, 2010a], and the intense spacecraft charging [*Denton and Borovsky*, 2012]. The fast wind after the stream interface is of coronal hole origin. The slow wind before the stream interface can be either helmet streamer origin plasma or pseudostreamer origin plasma.

[6] Helmet streamers form at the Sun when a loop arcade separates two coronal holes of opposite polarity [*Pneuman*, 1968; *Rusin et al*., 2010]. Pseudostreamers form when two like-signed coronal holes are separated by a pair of loop arcades [*Wang et al*., 2007; *Riley and Luhmann*, 2012]. More recent ideas posit that helmet streamers are formed by narrow open flux corridors through streamer belts on the Sun with the corridors connecting like-signed coronal holes [*Antiochos et al*., 2011; *Titov et al*., 2011; *Crooker et al*., 2012]. Away from the Sun, helmet streamers contain magnetic polarity reversals and pseudostreamers do not. Hence, at 1 AU, helmet streamer origin plasma is associated with a magnetic sector reversal and pseudostreamer origin plasma is not [*Crooker et al*., 2012]. Helmet streamer origin plasma and pseudostreamer origin plasma are both characterized by low proton-specific entropy $S_p = T_p/n_p^{2/3}$ and by high O^{7+}/O^{6+} and C^{6+}/C^{5+} density ratios [*Foullon et al*., 2011; *Wang et al*., 2012] (as opposed to coronal hole origin plasma which has high proton-specific entropy S_p and low O^{7+}/O^{6+} and C^{6+}/C^{5+} density ratios [*Siscoe and Intriligator*, 1993; *Zhao et al*., 2009]).

[7] A series of papers on the operation of the Earth's magnetosphere have been written based on superposed epoch analysis using 125 CIR-driven geomagnetic storms (also known as high-speed stream-driven storms) [e.g., *Denton and Borovsky*, 2008, 2012]. In the present paper, we examine those 125 CIR-driven storms and separate them into three categories: storms driven by helmet streamer CIRs, storms driven by pseudostreamer CIRs, and storms that are not categorized. The storms that are not categorized typically have significant intervals of ejecta plasma in the slow wind interval leading up to the CIR.

[8] In the present study, those 125 events are used for superposed epoch analysis of the reaction of the Earth's magnetosphere during helmet streamer CIR-driven storms and pseudostreamer CIR-driven storms. The observed systematic differences in the phenomenology of helmet streamer CIR storms versus pseudostreamer CIR storms are collected into Table 1. Particularly, for the preconditioning of the Earth's magnetosphere for the upcoming CIR storm, it makes a difference whether the slow wind preceding the CIR is of helmet streamer origin or of pseudostreamer origin.

[9] This manuscript is organized as follows. In section 2, the events, data sets, and data analysis methods are discussed. Section 3 examines the solar wind for both helmet streamer and pseudostreamer storms, and section 4 examines the magnetospheric driver functions for the two types of storms. Geomagnetic activity is studied in section 5, the plasmasphere and the drainage plumes are studied in section 6, the ion and electron plasma sheets in section 7, the geomagnetic field in section 8, and the outer electron radiation belt in section 9. The findings are summarized in section 10. Some unsolved issues are discussed in section 11.

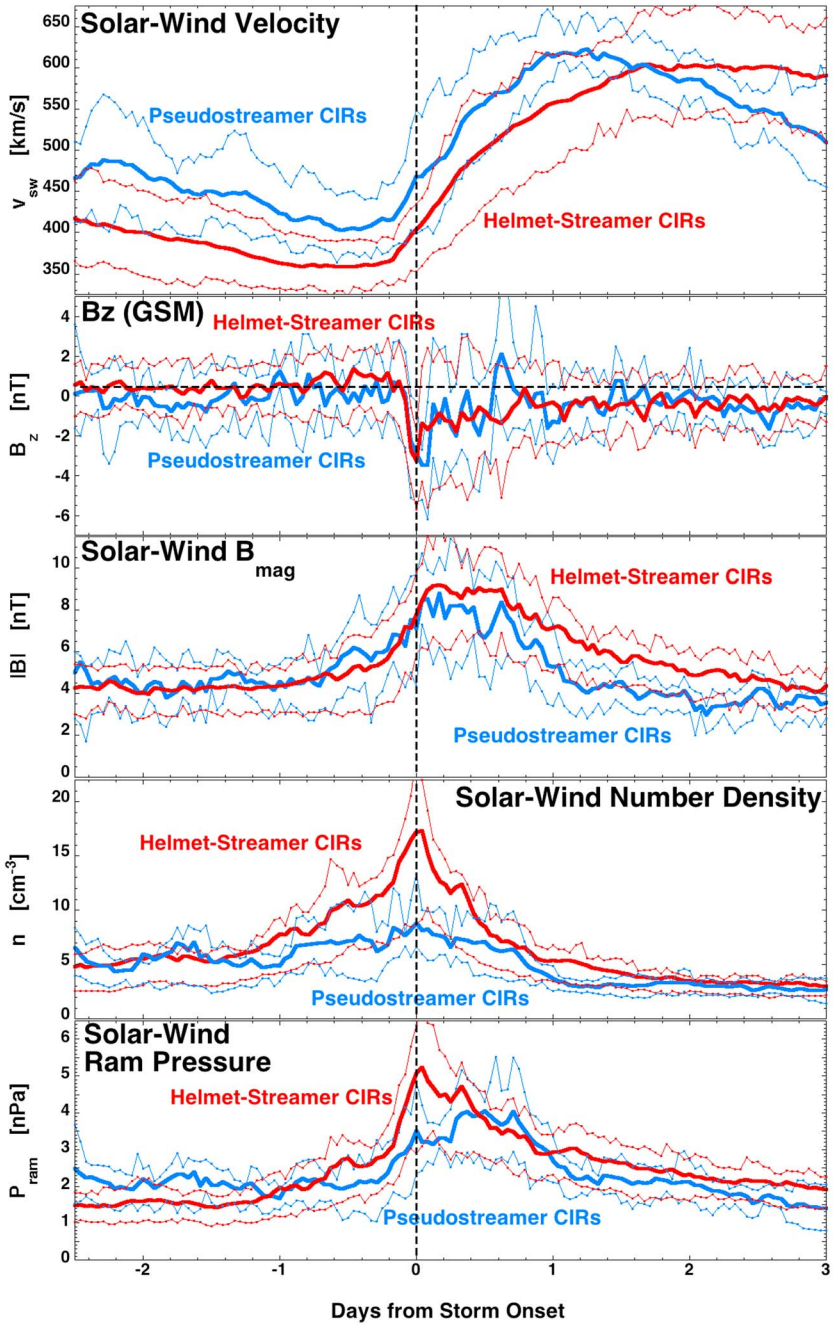

Figure 1. Superposed averages for several solar wind parameters with the zero epoch being the onset of storm levels of magnetospheric convection. The thick curves are mean values and the thin curves are upper and lower quartiles.

2. Events, Data Sets, and Data Analysis

[10] The 125 geomagnetic storms driven by helmet streamer CIRs and by pseudostreamer CIRs are obtained from a collection of 93 CIR-driven storms in 1995–2005 [cf. *Borovsky and Denton*, 2010a] plus a collection of 32 CIR-driven storms in 2005–2007 [*Denton and Borovsky*, 2012].

[11] For the 125 storms, the helmet streamer versus pseudostreamer nature of each CIR is determined from plots of the solar wind velocity v_{sw} (for locating 27 day repeating intervals of high-speed wind), the solar wind proton-specific entropy S_p (to determine coronal hole origin versus streamer belt origin plasma), the solar wind O^{7+}/O^{6+} and C^{6+}/C^{5+} density ratios (to determine coronal hole origin versus streamer belt origin plasma), the solar wind magnetic field azimuth angle in the ecliptic plane (to determine the IMF sector and to locate sector reversals), the solar wind magnetic field elevation angle out of the ecliptic plane (to help identify ejecta), the solar wind proton temperature (to help identify ejecta), and the intensity of the 272 eV electron flux in the solar wind as a function of pitch angle (to determine the IMF sector, to locate sector reversals, and to identify intervals of counterstreaming electron strahl to help identify ejecta). The

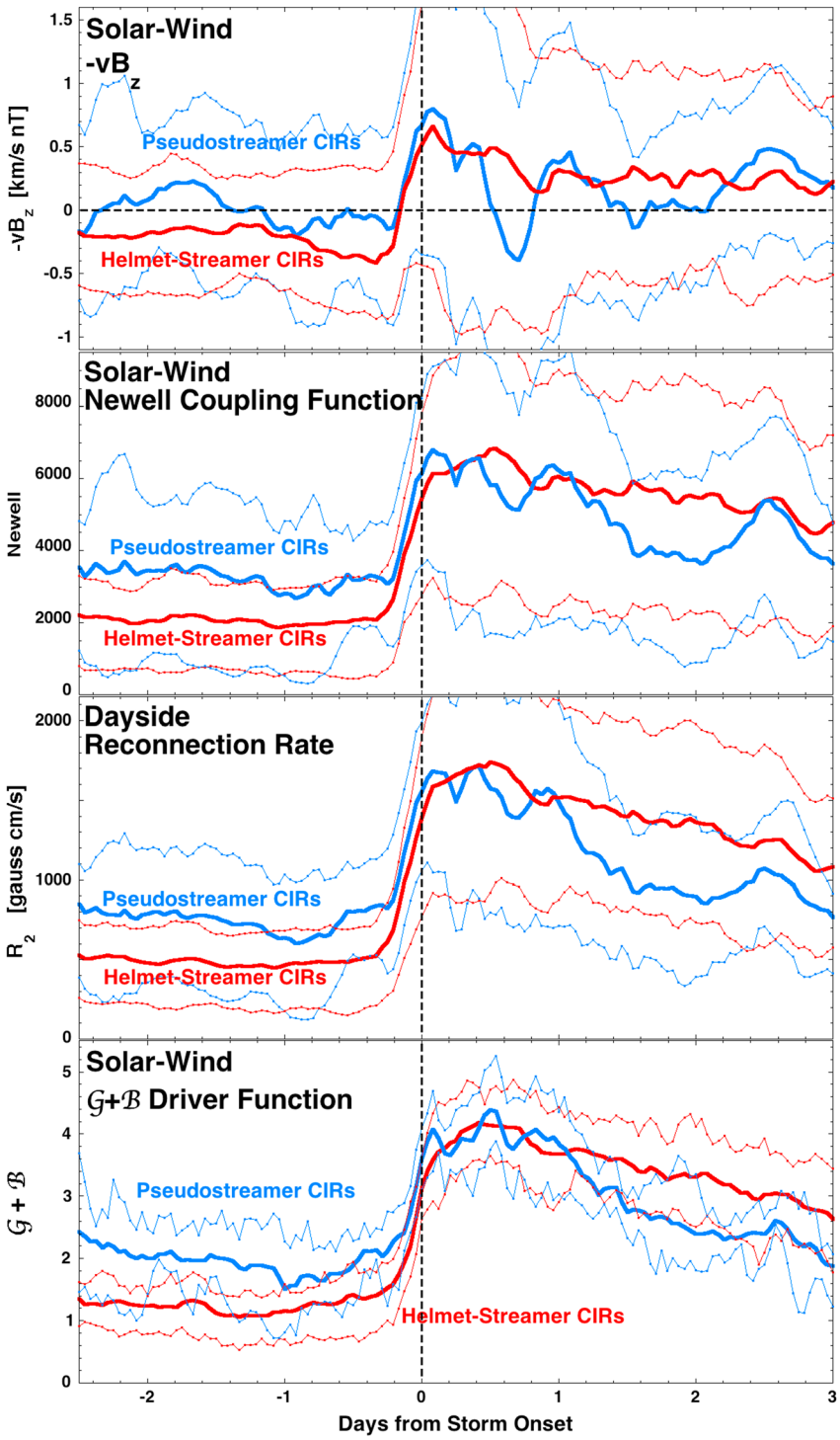

Figure 2. Superposed averages for four magnetospheric driver functions with the zero epoch being the onset of storm levels of magnetospheric convection. The thick curves are mean values and the thin curves are upper and lower quartiles.

data for these plots came from the OMNI2 data set [*King and Papitashvili*, 2005] and (after February 1998) from the Solar Wind Electron, Proton, and Alpha Monitor [*McComas et al.*, 1998], MAGnetometer Instrument (MAG) [*Smith et al.*, 1998], and Solar Wind Ion Composition Spectrometer [*Gloeckler et al.*, 1998] instruments onboard the ACE spacecraft at 1 AU. Pseudostremer CIRs and helmet streamer CIRs are identified in the time series measurements by the following five steps. (1) The CIR is identified as the compressed plasma on the leading edge of a coronal hole plasma high-speed stream with coronal hole origin plasma identified by high proton-specific entropy and low O^{7+}/O^{6+} and C^{6+}/C^{5+} density ratios. (2) The magnetic sector ("toward" or "away") of the coronal hole high-speed stream plasma that follows

the CIR is identified (either by the direction of the magnetic field with respect to the local Parker spiral direction or by the direction of the unidirectional electron strahl with respect to the magnetic field directions [*Crooker et al*., 2004a]). (3) Looking earlier in time at the plasma upstream of the CIR, the preceding interval of coronal hole origin high-speed wind is examined. If that preceding coronal hole is of the same magnetic sector as the coronal hole immediately following the CIR, and if no sector reversals occur in the streamer belt origin plasma between the two coronal holes, then the streamer belt plasma is identified as pseudostreamer origin plasma and the CIR is identified as a pseudostreamer CIR. (4) On the contrary, if the preceding coronal hole is of the opposite magnetic sector as the coronal hole immediately following the CIR, and if a sector reversals occurs in the streamer belt origin plasma between the two coronal holes, then the streamer belt plasma is identified as helmet streamer origin plasma and the CIR is identified as a helmet streamer CIR. (5) If there is obvious ejecta in between the two intervals of high-speed coronal hole origin wind (ejecta being identified as long intervals (~6 hr or more) having counterstreaming electron strahls, continuously out of ecliptic plane magnetic fields, and/or anomalously low proton temperatures [*Gosling et al*., 1973, 1987; *Richardson and Cane*, 1995; *Elliott et al*., 2005; *Skoug et al*., 2000]), then no categorization of the CIR type is made and that CIR is not used for the present study. Coronal mass ejections can be emitted from helmet streamers [e.g., *Foullon et al*., 2011] or from pseudostreamers [e.g., *Liu*, 2007].

[12] Of the 125 CIR-driven storms, 11 were clearly determined to be storms driven by pseudostreamer CIRs and 74 were clearly determined to be storms driven by helmet streamer CIRs. For the other 30 storms, clear categorizations could not be made.

[13] Superposed epoch analysis of the solar wind and of the magnetosphere is performed separately for these helmet streamer CIR-driven storms and these pseudostreamer CIR-driven storms using the onset of storm levels of magnetospheric convection as the zero epoch (trigger time). Each storm onset is determined from a temporal drop in the midnight boundary index (MBI) [cf. *Borovsky and Denton*, 2010a]. MBI is an index created from measurements of the location of the low-latitude edge of the diffuse auroral precipitation as determined by DMSP satellite overflights, mathematically shifted to local midnight [*Gussenhoven et al*., 1983]. MBI is a proxy for the position of the inner edge of the electron plasma sheet [*Elphic et al*., 1999], which makes it an excellent indicator of the strength of magnetospheric convection, as is *Kp* [*Thomsen*, 2004]. Storm onset is taken to be the time at which the MBI index drops rapidly. The storm onset times were determined at about 30 min accuracy.

[14] Data sets utilized in the superposed epoch analysis are as follows. For solar wind parameters, the OMNI2 1 min and 1 h data sets [*King and Papitashvili*, 2005] are used. For geomagnetic activity, the OMNI2 data set is again used. For the Earth's magnetic field at geosynchronous orbit and for the amplitude of ULF fluctuations at geosynchronous orbit, magnetometer data [*Dunham et al*., 1996] from the GOES-8 through GOES-12 series of spacecrafts [*Singer et al*., 1996] are used, with corrections for GOES-8 according to *Tsyganenko et al*. [2003]. To examine the state of the outer plasmasphere and the plasmaspheric drainage plumes, low-energy ion measurements from the multisatellite MPA (magnetospheric plasma analyzer) instrument [*Bame et al*., 1993] are used. For the ion and electron plasma sheets at geosynchronous orbit, ion and electron measurements from the multisatellite MPA instrument are used. For the state of the outer electron radiation belt, multisatellite SOPA (synchronous orbit particle analyzer) measurements [*Belian et al*., 1992; *Cayton and Belian*, 2007] at geosynchronous orbit are used, with relativistic bi-Maxwellian distribution functions fit to the SOPA count rates [*Cayton and Belian*, 2007] with the hotter Maxwellian population identified as the outer electron radiation belt [*Cayton et al*., 1989; *Belian et al*., 1996; *Denton et al*., 2010]. As in *Denton et al*. [2010], to reduce the influence of outliers when the measurements are noisy, median values of the radiation belt density and temperature are calculated for every 30 min of data and those half hour medians are used.

3. The Solar Wind for Helmet Streamer CIR Storms and Pseudostreamer CIR Storms

[15] In Figure 1, the superposed averages of several solar wind parameters are plotted. In each panel, the red curve is the superposed average for 74 storms driven by helmet streamer CIRs and the blue curve is the superposed average for 11 storms driven by pseudostreamer CIRs. In each case, the zero epoch (vertical dashed line) is the onset of storm levels of magnetospheric convection. The plots extend from 2.5 days before storm onset to 3 days after storm onset.

[16] In the top panel of Figure 1, the superposed average of the solar wind speed v_{sw} is plotted as the thick curves and the upper and lower quartiles are plotted as the thin curves with points. For both types of storms, the transition of slow wind before the storm onset to fast wind after the storm onset is seen. Note that the solar wind on average is slower before the storm for helmet streamer CIRs than it is for pseudostreamer CIRs: this can be seen by looking at the averages (thick curves) or by looking at the upper or lower quartiles (thin curves). The difference in wind speed is noted in line 2 of Table 1. Having looked at large numbers of helmet streamer CIRs and pseudostreamer CIRs besides these that drive well-developed storms, it is the strong impression of the authors that the helmet streamer wind prior to CIR stream interfaces tends to be noticeably slower than the pseudostreamer wind prior to CIR stream interfaces; this difference in the speed of the wind has been reported before for CIRs with and without sector reversals [*Neugebauer et al*., 2004], and see also *Crooker and McPherron* [2012]. Note in the top panel of Figure 1 that in the days after storm onset, the wind speed remains higher on average for the helmet streamer CIRs than it does for the pseudostreamer CIRs: this may be an indication that the coronal hole associated with a helmet streamer is larger on average than the coronal hole associated with a pseudostreamer. This difference is noted in line 3 of Table 1. The difference in the duration of the fast wind has been reported before for CIRs with and without sector reversals [*Neugebauer et al*., 2004].

[17] In the second panel of Figure 1 the superposed average of the solar wind magnetic field component B_z in GSM coordinates is plotted. For both types of storms, B_z is on average southward (negative) at the time of storm onset and after storm onset. (If this were not the case, a storm probably would not be driven and the event probably would

not have been selected.) For the helmet streamer CIR storms (red curve), the superposed average of B_z is steadily northward before the storm; for the pseudostreamer CIR storms (blue curve), the superposed average of B_z is northward and southward before the storm. CIR-driven storms are associated with the Russell-McPherron effect [*Russell and McPherron*, 1973] wherein the Parker spiral orientation solar wind can have on average a magnetic field that is southward in the frame of the Earth's dipole (GSM coordinates) owing to the tilt of the dipole relative to the solar equatorial plane and the dipole toward or away from the sector of the IMF. If there is a CIR-driven storm, then it is likely that the magnetic sector of the high-speed stream following the stream interface is Russell-McPherron effective [*Borovsky and Steinberg*, 2006; *McPherron et al*., 2009; *Kissinger et al*., 2011]. As noted in line 1 of Table 1, helmet streamers have sector reversals and pseudostreamers do not. If that CIR is led by helmet streamer plasma, then there will be a sector reversal in the helmet streamer plasma, and ahead of that sector reversal, the solar wind will be Russell-McPherron ineffective having a northward component in the reference frame of the Earth's dipole. Hence, the pre-storm positive B_z in Figure 1 is the superposed average for the helmet streamer CIR storms. This Russell-McPherron ineffectiveness leads to the commonly occurring "calm before the storm" [*Borovsky and Steinberg*, 2006]. This scenario is not the case for pseudostreamer CIRs, which do not have sector reversals in the pseudostreamer plasma. If the fast wind following the CIR is Russell-McPherron effective with an on-average southward field, then the pseudostreamer slow wind ahead of the CIR will also be Russell-McPherron effective with an on-average southward field. As will be seen in section 3, this will result in a non occurrence of the calm before the storm for pseudostreamer CIR storms.

[18] Note, the streamer belt plasma and the coronal hole plasma both have Parker spiral field orientations; if it were not for tilt of the Earth's dipole, for geomagnetic activity, it would be irrelevant whether or not there is a sector reversal between the slow and fast wind.

[19] In the third panel of Figure 1, the superposed average of the solar wind magnetic field strength B_{mag} is plotted for the two types of storms. In the coronal hole origin high-speed wind a day or so after the onset of the storms, the magnetic field strength is on average about the same for the helmet streamer CIRs as it is for the pseudostreamer CIRs. Within the CIRs (around the time of storm onset), the magnetic field strength is elevated for both types of CIRs. This field strength being elevated above the field strength of the high-speed wind is owed to the compression of the plasma in the CIR, and the ratio of the field strength in the CIR to the field strength in the high-speed wind outside the CIR can be used as a measure of the strength of the compression [*Borovsky and Denton*, 2010b]. This solar wind magnetic field strength ratio for the collection of pseudostreamer CIRs about the same as the ratio of the solar wind magnetic field strength in the collection of helmet streamer CIRs; by that measure, the solar wind compression of the pseudostreamer CIRs is about the same as the solar wind compression of the helmet streamer CIRs: both are strong. This is noted in line 4 of Table 1. Note in the third panel of Figure 1 that the field strength in the pseudostreamer slow wind in the days before the storm onset is about the same as the magnetic field strength in the helmet streamer slow wind in the days before the storm onset.

[20] In the fourth panel of Figure 1, the superposed average of the number density n of the solar wind is plotted as the thick curves and the upper and lower quartiles are plotted as the thin curves with points. Note the considerable difference at the time of storm onset: the number density in the CIR is quite elevated on average inside the helmet streamer CIRs but not in the pseudostreamer CIRs; this can be seen in the average and in the quartiles. This might be expected for the properties of helmet streamers, which are known to be associated with the emission of blobs of dense plasma near the Sun [*Wang et al*., 2000; *Foullon et al*., 2011]. This is also expected for plasma with sector reversals, with the dense heliospheric plasma sheet often seen at the sector reversal current sheet [*Winterhalter et al*., 1994; *Crooker et al*., 2004b]. On the contrary, pseudostreamers are known not to emit plasma blobs near the Sun [*Wang et al*., 2012]. This difference in the solar wind number density for CIRs with and without sector reversals has been reported by *Neugebauer et al*. [2004]. This difference is noted in line 5 of Table 1.

[21] In the bottom panel of Figure 1, the superposed average of the solar wind ram pressure $P_{ram} = \rho v_{sw}^2$ is plotted for the two types of storms. In the days before the storm, the ram pressure is lower on average for the helmet streamer CIR storms, probably because the solar wind velocity v_{sw} is lower on average before the helmet streamer CIR storms. At time of storm onset, the ram pressures for the two types of storms are elevated with the helmet streamer storms larger. The elevated ram pressure for the two types of storms is noted in line 6 of Table 1.

4. Magnetospheric Driver Functions for Helmet Streamer CIR Storms and Pseudostreamer CIR Storms

[22] In Figure 2, the superposed averages of four solar wind/magnetosphere coupling functions are plotted as functions of time for the two types of CIR-driven storms. As always, time $t = 0$ (vertical dashed line) is the onset of storm levels of geomagnetic activity. In the top panel, $-vB_z$ of the solar wind is plotted, where v is the total solar wind speed and B_z is the GSM north-south component of the solar wind magnetic field. In the second panel of Figure 2, the *Newell et al*. [2007] coupling function $v^{4/3}B_\perp^{2/3}\sin^{8/3}(\theta/2)$ is plotted, where $B_\perp$ is the component of the solar wind magnetic field $\underline{B}$ that is perpendicular to the Sun-Earth line and where θ is the clock angle of the magnetic field relative to the Earth's dipole ($\theta = 0^o$ for a purely northward IMF and $\theta = 180^o$ for a purely southward IMF). In the third panel, the *Borovsky* [2013] reconnection control function R_2 is plotted, where R_2 depends on n, v, and M_A ($M_A = v/v_A$ is the Alfven Mach number) of the solar wind and on the clock angle of the IMF. In the bottom panel, the G + B driver function of J. E. Borovsky (Physics based solar-wind driver functions for the magnetosphere: Combining the reconnection-coupled MHD generator with the viscous interaction, submitted to *Journal of Geophysical Research*, 2013b) is plotted where G is the "reconnection-coupled MHD generator" and B is a Bohm viscosity viscous interaction driver. Upper and lower quartiles are also plotted (thin lines with points) in the bottom panel. In all four plots

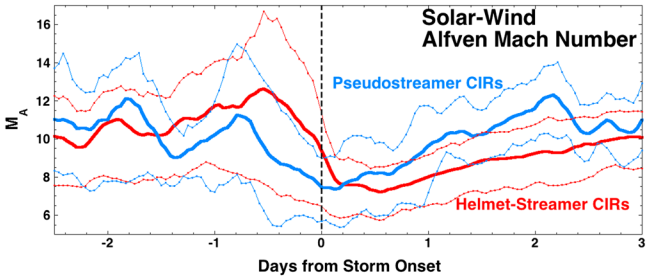

Figure 3. The superposed average of the Alfven Mach number of the solar wind, with the zero epoch being the onset of storm levels of magnetospheric convection. The thick curves are mean values and the thin curves are upper and lower quartiles.

of Figure 2, stronger driving is upward on the graph and weaker driving is downward.

[23] In the top panel, prior to storm onset, the helmet streamer CIR storms exhibit a definite northward bias ($-vB_z < 0$) while the pseudostreamer CIR storms exhibit a slightly southward bias ($-vB_z > 0$). Accordingly, prior to storm onset, the driving of the magnetosphere should be weaker for the helmet streamer CIR storms than for the pseudostreamer CIR storms. The driving functions plotted in the second, third, and fourth panels of Figure 2 also predict a weaker pre-storm driving for helmet streamer CIR storms than for pseudostreamer CIR storms. In the bottom panel, this can also be seen in the upper and lower quartiles as well as in the mean.

[24] In the first day or so after storm onset, all four driver functions plotted in Figure 2 indicate a similar strength of driving for helmet streamer CIR storms as for pseudostreamer CIR storms.

[25] From top to bottom in Figure 2, the driver functions become smoother. After the first day of the storm, the Newell, R_2, and G + B coupling functions clearly predict weaker driving for pseudostreamer storms than for helmet streamer storms. This is also borne out by the upper and lower quartiles in the bottom panel.

[26] In Figure 3, the superposed average of the Alfven Mach number $M_A = v/v_A$ of the solar wind is plotted for the two types of CIR-driven storms as the thick curves and the upper and lower quartiles are plotted as the thin curves with points. A critical Mach number occurs at $M_A = 6$: the plasma beta of the magnetosheath can be parameterized as $\beta_s = (M_A/6)^{1.92}$ [cf. *Borovsky*, 2008, equation (13a)]. If M_A is greater than 6, then β_s is greater than unity: at very high beta, the magnetosheath flows according to gas dynamics [*Spreiter and Stahara*, 1994]. If M_A is less than 6, then β_s is less than unity; at low beta, the magnetosheath flow has MHD effects, including jetting and anisotropic pressure resulting in magnetospheric flattening and changes in the magnetopause Kelvin-Helmholtz instabilities [*Lavraud and Borovsky*, 2008]. In Figure 3, the superposed averages of the values of M_A are always >6; however, according to the lower quartiles, there are some CIR storms that have M_A values less than 6 during the time of CIR passage (from t = −1 day to t = +1 day). Note that for most of the duration of the storm, the Alfven Mach number of the solar wind is consistently lower for helmet streamer CIR storms than it is for pseudostreamer CIR storms, a trend that can be seen in the averages or in the upper or lower quartiles. This Mach number difference is noted in line 7 of Table 1.

5. Geomagnetic Activity

[27] In Figure 4, the superposed averages of three geomagnetic indices are plotted for the two types of CIR-driven storms. In the top panel, the superposed average of the *Kp* index is plotted as the thick curves and the upper and lower quartiles are plotted as the thin curves with points. Note the difference in the *Kp* profile for the two types of storms. First, in the days before storm onset, the *Kp* index is lower on average for the helmet streamer storms than it is for the pseudostreamer storms. The mean value of *Kp* for all times is *Kp* = 2.3, and the superposed average of *Kp* is substantially lower than 2.3 before the helmet streamer CIR storms. This is the well-known "calm before the storm" [*Borovsky and Steinberg*, 2006] which occurs prior to 66% of all CIR-driven storms. Note that *Kp* is on average just slightly lower than 2.3 before the pseudostreamer CIR storms: the pseudostreamer CIR storms do not on average exhibit the calm before the storm. This calm versus no-calm dichotomy can be reasoned by examining B_z (GSM) in the second panel of Figure 1; B_z is definitely northward on average before the helmet streamer CIR storms leading to the calm before the storm behavior. The weakness of the driver functions in Figure 2 for helmet streamers also reflects this difference of calm versus no calm. This calm/no-calm difference in the two types of storms is noted in line 8 of Table 1.

[28] In the *Kp* plot of the top panel of Figure 4, the *Kp* value after the first day of the storm is on average weaker for the pseudostreamer CIR storms than it is for the helmet streamer CIR storms. This probably reflects the larger coronal holes following helmet streamers (cf. top panel of Figure 1). The driver functions of Figure 2 also show this trend. This similarity in the strength of the storms is noted on line 9 of Table 1.

[29] In the middle panel of Figure 4, the superposed average of the northern polar cap index (PCI) is plotted for the two types of CIR-driven storms. Similar to the behavior of *Kp* in the top panel, PCI is on average lower before the storm for helmet streamer storms than it is for pseudostreamer storms, reflecting an absence of calms before the storms for pseudostreamer CIR storms. And similar to the *Kp* index, later in the storms, PCI is lower for the pseudostreamer CIR storms than for the helmet streamer CIR storms.

[30] In the bottom panel of Figure 4, the superposed average of the pressure-corrected *Dst* index *Dst** is plotted for the two types of storms. In *Borovsky and Denton* [2010b], a fit of measured values of *Dst* and the square root of the solar wind ram pressure in the period prior to geomagnetic activity

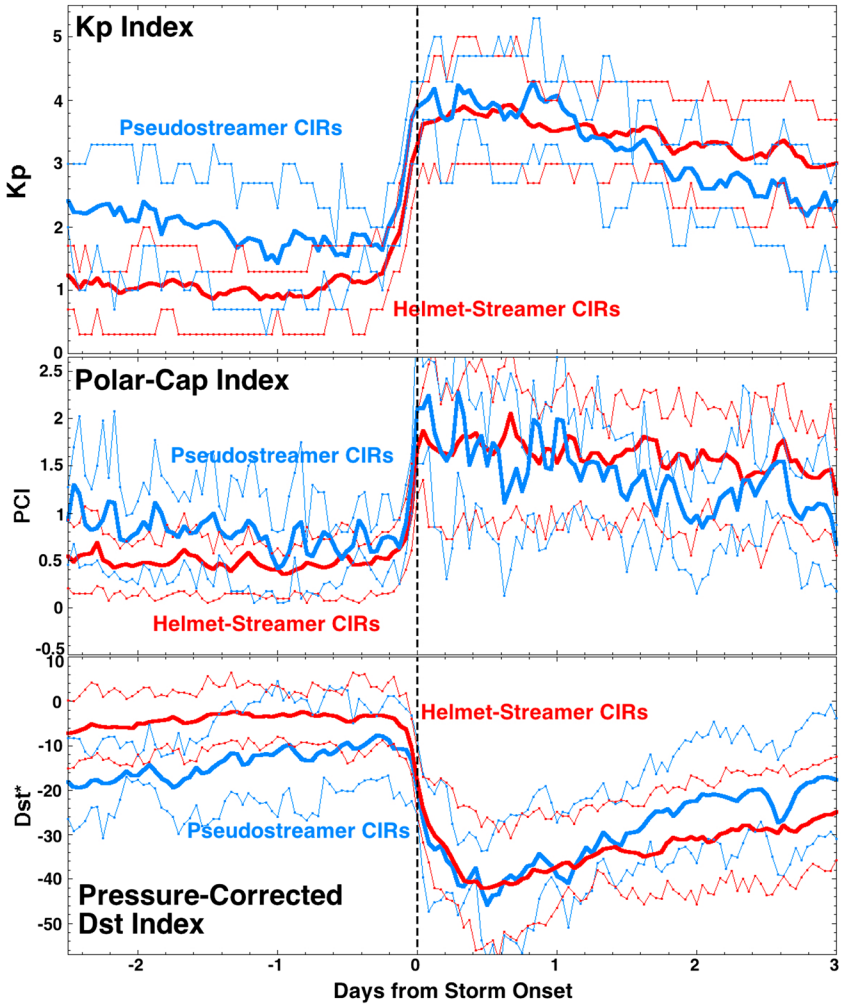

Figure 4. Superposed averages for three geomagnetic indices with the zero epoch being the onset of storm levels of magnetospheric convection. The thick curves are mean values and the thin curves are upper and lower quartiles.

commencing in CIR-driven storms yielded the *Dst* correction formula $Dst^* = Dst - bP_{ram}^{1/2} + c$ with the coefficients $b = 20.7$ nT $(\text{nPa})^{-1/2}$ and $c = 27.7$ nT, where *Dst** and *Dst* are in units of nT and $P_{ram} = \rho v^2$ is in units of nanopascal. This formula is used to produce the *Dst** values that are superposed in the bottom panel of Figure 4. Before the storm, *Dst** is on average near zero for the helmet streamer CIR storms (with their calms before the storms) while it is in a slightly elevated (negative) state on average for the pseudostreamer CIR storms with magnetospheric driving ongoing before storm onset. Early in the storm, the *Dst** values are similar, whereas later in the storm, *Dst** is on average weaker for the pseudostreamer CIR storms than for the helmet streamer CIR storms. This similarity of the *Dst* perturbations is noted in line 10 of Table 1.

6. The Plasmasphere and Drainage Plumes

[31] In Figure 5, the superposed average of the cold ion (<100 eV) number density at geosynchronous orbit (6.6 R_E) averaged over all local time is plotted for the two types of storms. Prior to storm onset, the average cold ion number density for the helmet streamer CIR storms is substantially higher than the average number density for the pseudostreamer CIR storms. This reflects the fact that helmet streamer CIR storms tend to have calms before the storms (cf. Figure 4), whereas pseudostreamer CIR storms do not. During a calm before the storm, the outer plasmasphere refills [*Borovsky and Steinberg*, 2006; *Denton and Borovsky*, 2008], which results in a more filled outer plasmasphere prior to helmet streamer CIR storms but not prior to pseudostreamer CIR storms. This difference in the pre-storm plasmasphere is noted in line 11 of Table 1. Note before the storm onset that the mean values of the cold ion number density in Figure 5 are near or above the upper quartile values, particularly for the pseudostreamer CIRs; this is caused by skewness in the density distribution where many very low values are obtained and only a few very large values, which set the mean.

[32] During the storm, the local time averaged cold ion number density picks up the plasmaspheric drainage plume in the 12–18 LT sector [*Borovsky and Denton*, 2008], with all other regions of local time being void of cold ions at geosynchronous orbit during the storm [*Denton and Borovsky*, 2008]. Since only a minority of the density measurements

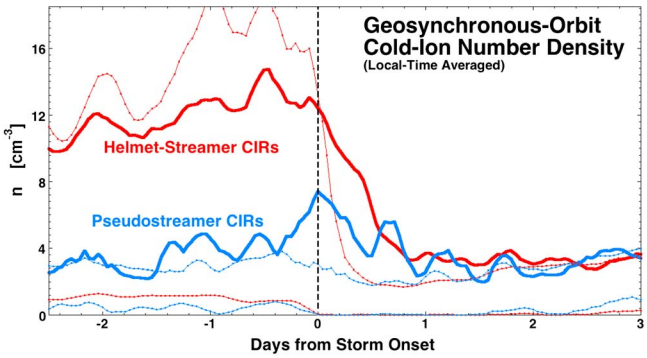

Figure 5. The superposed average of the plasmaspheric number density at geosynchronous orbit, averaged over all local times. The zero epoch being the onset of storm levels of magnetospheric convection. The thick curves are mean values and the thin curves are upper and lower quartiles.

around local time shows the high-density plume and the high-density of the plume drives the mean value, the mean value tends to be above the upper quartile during the storm. Figure 5 shows that during the storms, the local time averaged number density is on average about the same for the two types of storms. This means that the product of the number density times the local time width of the drainage plumes is about the same for the two types of storms. Looking at the flow velocity of the plume plasma, the authors find the two types of storms to yield similar flow velocities. Hence, the amount of mass flow in the plumes is approximately equal for the two types of storms. This similarity in the strengths of the drainage plumes for the two types of storms is noted in line 12 of Table 1. This similarity is somewhat contrary to expectations [cf. *Borovsky and Denton*, 2008]: if the outer plasmasphere was more filled prior to helmet streamer CIR storms than it was prior to pseudostreamer CIR storms, one would expect to be draining more plasma for helmet streamer CIR storms and hence to be having higher-density drainage plumes for helmet streamer CIR storms.

7. The Ion and Electron Plasma Sheet

[33] In Figure 6, several plasma sheet parameters measured at geosynchronous orbit are plotted for the two types of storms. In the top panel, the superposed average of the number density of hot electrons (>100 eV) is plotted, averaged over the nightside local times 21–3 LT. The electron plasma sheet density is only plotted on the nightside of geosynchronous orbit: the hot electrons of the plasma sheet do not survive convection to the dayside and duskside at geosynchronous orbit, and they are strongly decaying on the dawnside [*Thomsen et al.*, 1998; *Denton et al.*, 2005]. For both types of storms, there is an enhanced hot electron density that commences before storm onset: this is the electron plasma sheet going into its superdense phase [*Borovsky et al.*, 1997] early in the storm. On average, the superdense phase is more robust for the helmet streamer CIR storms (red) than for the pseudostreamer CIR storms (blue). This is noted in line 13 of Table 1. This greater density of the plasma sheet for helmet streamer storms is associated with the greater solar wind density (fourth panel of Figure 1) for helmet streamer storms, since the plasma sheet density is directly related to the solar wind density with a time lag [*Borovsky et al.*, 1998a; *Denton and Borovsky*, 2009].

[34] In the second and third panels of Figure 6, the superposed average of the hot ion (>100 eV) number density at geosynchronous orbit is plotted on the nightside (21–3 LT) and on the dayside (9–15 LT) for the two types of storms. In the figure, the ion plasma sheet exhibits a superdense phase early in the storm, with the superdense plasma sheet reaching the nightside (second panel) before it reaches the dayside (third panel), with a characteristic convection time of 7–11 h from the nightside to the dayside [*Borovsky et al.*, 1998a; *Denton and Borovsky*, 2009]. In the second and third panels, the superdense phase of the ion plasma sheet is weaker for pseudostreamer CIR storms than it is for helmet streamer CIR storms. Again, this weaker density is owed to a weaker solar wind density for pseudostreamer storms than for helmet streamer storms (fourth panel of Figure 1).

[35] In the fourth and fifth panels of Figure 6, the superposed averages of the electron plasma sheet and ion plasma sheet temperatures are plotted for the two types of storms. The electron temperature is an average over the nightside local times 21–3 LT, and the ion temperature is an average over all local times. The reader should note that the ion temperatures measured by the MPA instrument at geosynchronous orbit are underestimates typically by about a factor of 2, owing to the fact that the ion plasma sheet contains a significant number of ions with energies above the 45 keV limit of the MPA detector [cf. *Borovsky et al.*, 1998b]. In both the fourth and fifth panels, it is seen that the ion and electron plasma sheet temperatures increase substantially at storm onset and remain elevated for days. This is the "extra hot" phase of the plasma sheet during storms driven by high-speed solar wind following the CIR [*Denton and Borovsky*, 2009]. The fact that both types of storms exhibit the extra hot phase is indicated in line 14 of Table 1. Note in the fourth and fifth panels of Figure 6 that the average temperatures of the electron and ion plasma sheets are already somewhat elevated before the storm for pseudostreamer CIR storms (relative to the average temperatures for the helmet streamer CIR storms). This elevated temperature is probably related to (a) ongoing activity before the pseudostreamer storms (cf. Figure 4) and (b) a higher-velocity solar wind before the pseudostreamer storms (cf. top panel of Figure 1).

[36] In the bottom panel of Figure 6, the superposed average of the spacecraft potential with respect to infinity as measured by the MPA detectors in geosynchronous orbit

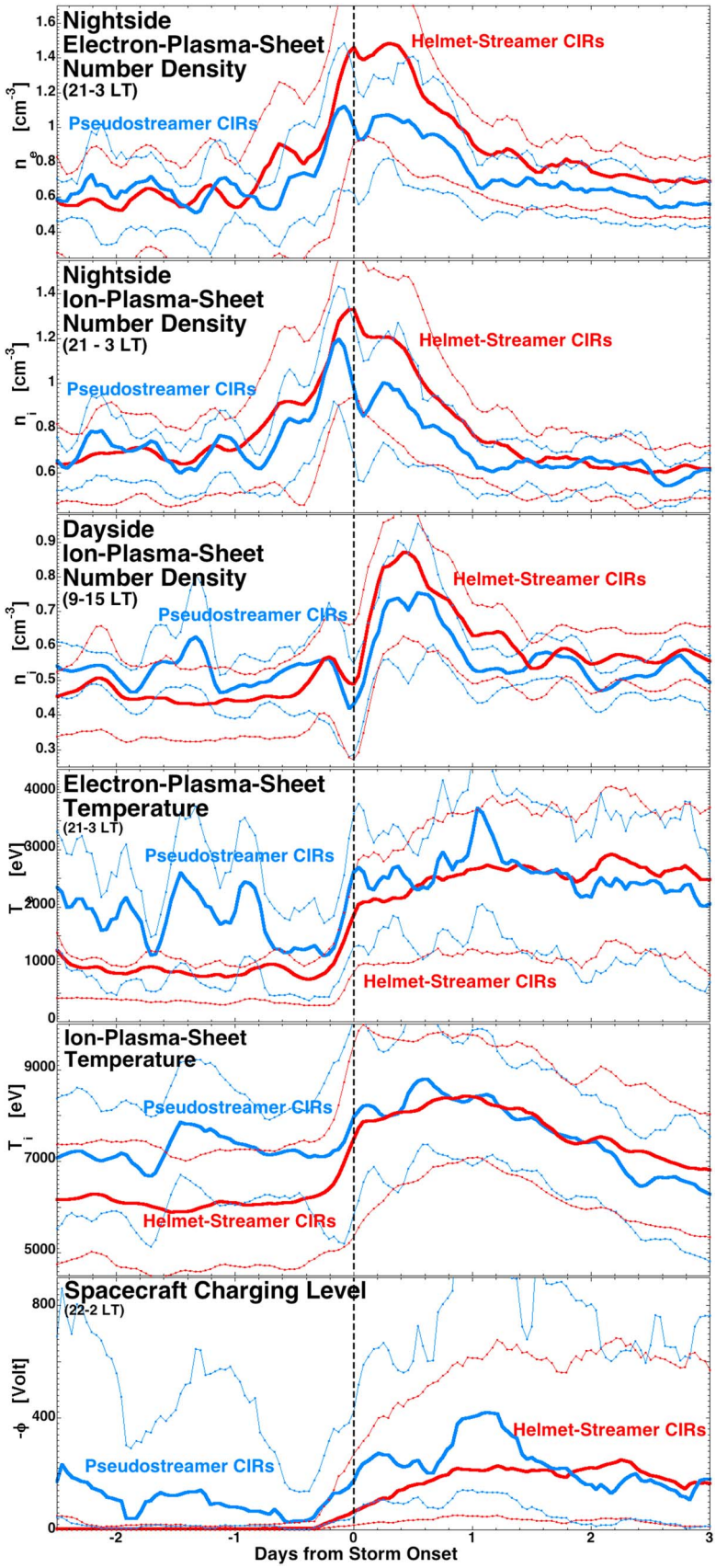
Nightside
Electron-Plasma-Sheet
Number Density
(21-3 LT)
Helmet-Streamer CIRs
Pseudostreamer CIRs
Nightside
Ion-Plasma-Sheet
Number Density
(21 - 3 LT)
Helmet-Streamer CIRs
Pseudostreamer CIRs
Dayside
Ion-Plasma-Sheet
Number Density
(9-15 LT)
Helmet-Streamer CIRs
Pseudostreamer CIRs
Electron-Plasma-Sheet
Temperature
(21-3 LT)
Pseudostreamer CIRs
Helmet-Streamer CIRs
Ion-Plasma-Sheet
Temperature
Pseudostreamer CIRs
Helmet-Streamer CIRs
Spacecraft Charging Level
(22-2 LT)
Helmet-Streamer CIRs
Pseudostreamer CIRs
Days from Storm Onset

Figure 6

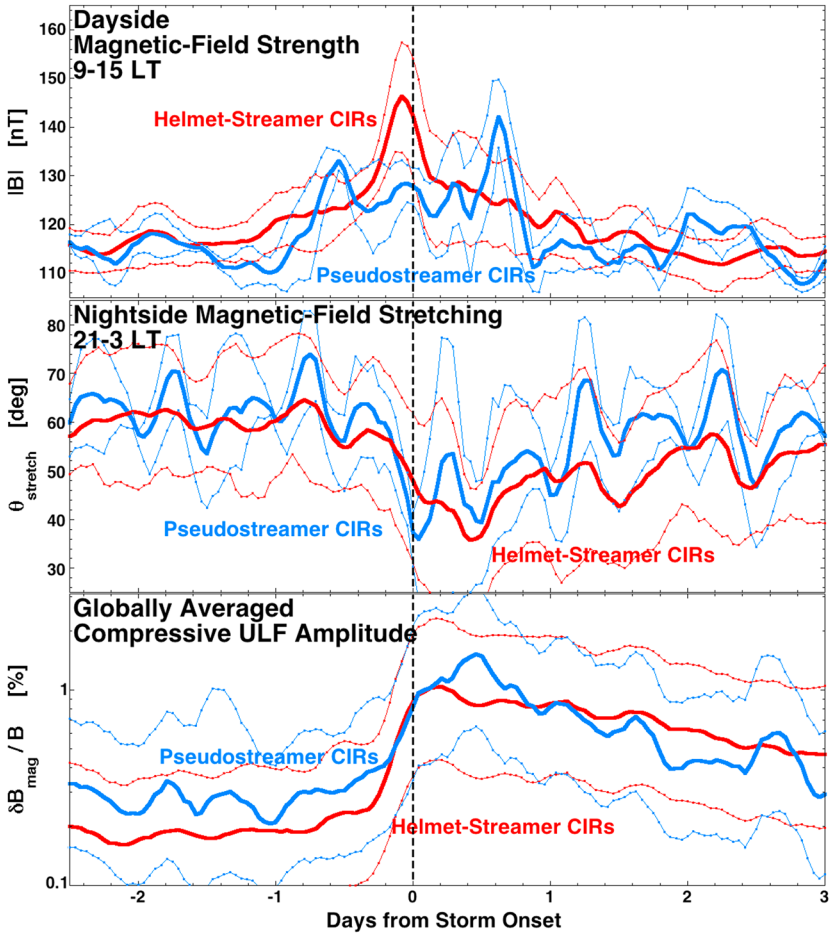

Figure 7. Superposed averages of properties of the geomagnetic field at geosynchronous orbit, with the zero epoch being the onset of storm levels of magnetospheric convection. The thick curves are mean values and the thin curves are upper and lower quartiles.

is plotted for the two types of storms. The spacecraft potential is obtained from a measure of the energy of the cold ion line [*DeForest*, 1972; *Thomsen et al.*, 1999]. The charging measurements are averaged over a near-midnight band of local time 22–2 LT. It is seen that for both types of storms, the level of spacecraft charging in the electron plasma sheet increases at storm onset and is high for days after the onset of the storm. (This is noted in line 15 of Table 1.) This high level of spacecraft charging reflects the extra hot electron plasma sheet temperature seen in the fourth panel of Figure 6. For the helmet streamer CIR storms, the level of spacecraft charging is low prior to onset (when the calm before the storms are ongoing): this also reflects the lower electron temperature for those events. Prior to storm onset, the levels of spacecraft charging for pseudostreamer CIR storms is moderate, reflecting the elevated electron temperatures prior to those storms.

8. The Geomagnetic Field

[37] In Figure 7, some parameters of the geomagnetic field measured at geosynchronous orbit are plotted for the two types of storms. In the top panel, the superposed average of the magnetic field strength in the dayside sector 9–15 LT is plotted. For the helmet streamer CIR storms (red), a distinct compression of the magnetic field strength on the dayside is seen just prior to storm onset with the on-average strength going from ~125 to ~150 nT. For the helmet streamer CIR storms, the geosynchronous orbit dayside magnetic field strength rises about the same time that the solar wind ram pressure rises (cf. bottom panel of Figure 1); however, the dayside field strength declines well before the ram pressure declines. This early decline has been explored in a prior survey [*Borovsky and Denton*, 2010b] of the geosynchronous magnetic field during CIR-driven storms, and it has been argued that the early decline of the dayside magnetic

Figure 6. Superposed averages of several hot plasma parameters at geosynchronous orbit, plus the superposed average of the spacecraft potential. The zero epoch being the onset of storm levels of magnetospheric convection. The thick curves are mean values (except for the bottom panel where they are median values) and the thin curves are upper and lower quartiles.

field strength is owed to diamagnetic reduction of the field strength when the superdense plasma sheet arrives in the dayside magnetosphere. In the third panel of Figure 6, for helmet streamer CIR storms, the superdense ion plasma sheet arrives in the dayside magnetosphere at about the time that the dayside field strength declines.

[38] For pseudostreamer CIR storms, this compression of the dayside magnetic field strength (top panel of Figure 7) is weaker and is delayed in time, as is the ram pressure of the solar wind is approximately as strong as it is for helmet streamer CIR storms (bottom panel of Figure 1). The low number of events (11) in the superposed epoch analysis (with only 2 GOES satellites taking data at any time and those two being in a limited range of longitude) results in a high noise level for the blue curve. Clearly, a larger number of pseudostreamer CIR storm events would be desirable. This difference in the dayside magnetic field strength for the two types of storms is noted in line 16 of Table 1.

[39] In the middle panel of Figure 7, the stretching angle $\theta_{stretch}$ of the magnetic field in the nightside sector (21–3 LT) of geosynchronous orbit is plotted. The notation is that the stretching angle $\theta_{stretch} = 90^o$ for a pure dipolar configuration and $\theta_{stretch} = 0^o$ for a purely radial field. In the middle panel, both types of storms exhibit a strong nightside stretching in the early portions of the storm, with the stretching decaying faster after storm onset for the pseudostreamer CIR storms than it does for the helmet streamer CIR storms. This strong stretching for both types of storms is noted in line 17 of Table 1.

[40] In the bottom panel of Figure 7, the superposed average of the fractional amplitude $\delta B_{mag}/B_{mag}$ of compressive ULF oscillations at geosynchronous orbit is plotted, averaged over all local times. The quantity δB_{mag} is the 1 min change in the strength of the magnetic field $\delta B_{mag}(t) = B_{mag}(t + 1\ min) - B_{mag}(t)$ where $B_{mag} = |\underline{B}| = (B_x^2 + B_y^2 + B_z^2)^{1/2}$. The denominator B_{mag} in $\delta B_{mag}/B_{mag}$ is $[B_{mag}(t + 1\ min) + B_{mag}(t)]/2$. Looking at 1 min changes, the measurement is most sensitive to changes with 1 min temporal gradients or sinusoidal fluctuations with periods on the order of 1.5–5 min. In the bottom panel, for both types of storms, the amplitude of compressive ULF fluctuations greatly increases at the time of storm onset and then declines slowly in the days after onset. The decline is faster for the pseudostreamer CIR storms than it is for the helmet streamer CIR storms; this difference in declines of the ULF amplitudes may be associated with the difference in declines of the solar wind speed in the high-speed streams following the CIRs, with the solar wind speed falling off faster for pseudostreamer CIR storms (cf. top panel of Figure 1). This strong enhancement in the amplitude of ULF fluctuations for both types of storms is noted in line 18 of Table 1.

9. The Outer Electron Radiation Belt

[41] In Figure 8, several parameters related to the outer electron radiation belt at geosynchronous orbit are plotted for the two types of storms. In the top panel, the superposed average of the number density of the outer electron radiation belt at geosynchronous orbit averaged over all local times is plotted. For helmet streamer CIR storms (red), in the days prior to storm onset, the number density of the outer radiation belt shows a characteristic exponential decay with time. This pre-storm decay has been associated with the occurrence of the calm before the storm and the presence of a built-up outer plasmasphere [*Borovsky and Denton*, 2009b]: the helmet streamer CIR storms which show this decay are characterized both by a calm before the storm (cf. Figure 4) and a built-up outer plasmasphere during the calm (cf. Figure 5). In the days before storm onset, the pseudostreamer CIR storms do not show as clear an exponential pre-storm decay in the top panel of Figure 8, probably owing to the absence on average of a calm before the storm and the absence on average of a built-up outer plasmasphere before the storm. More events will be needed to firmly conclude that pseudostreamer CIR storms lack the exponential pre-storm decay of the radiation belt. This potential difference in the pre-storm decay of the outer electron radiation belt is noted for these two types of storms in line 19 of Table 1.

[42] As can be discerned in the top panel of Figure 8, near the time of storm onset, the outer electron radiation belt exhibits a density dropout, which is a strong rapid drop in the number density [*Denton et al*., 2010]. Both types of storms exhibit this density dropout, with the number density of the helmet streamer CIR storms starting at lower values and going down to lower values than the pseudostreamer CIR storms. This deeper drop for helmet streamer storms might be owed to a stronger ram pressure for helmet streamers (cf. bottom panel of Figure 1). This difference in the depth of the density dropout is noted in line 20 of Table 1. About 6 h or so after the density drops, the number density suddenly increases and within a day, the density recovers to a new level that then persists for days. The number density at recovery is about the same for the two types of storms. For the helmet streamer CIR storms, the recovered radiation belt density in the storm is greater than the density before the storm (because of the pre-storm decay of the density); for the pseudostreamer CIR storms, the radiation belt number density after recovery is on average about the same as the density before dropout.

[43] In the second panel of Figure 8, the superposed average of the temperature of the outer electron radiation belt is plotted, averaged over all local times. For both types of storms, the temperature of the radiation belt is approximately constant with time in the days before storm onset (while the number density may or may not decay). Early in the storm at the time of density recovery, the temperature drops for both types of storms. This has been interpreted as a new denser population of radiation belt electrons appearing at geosynchronous orbit with a temperature somewhat cooler than the typical temperatures for the radiation belt [*Borovsky and Denton*, 2010a, 2011]. During the storms, the temperature of the electron radiation belt steadily increases for both types of storms. The value found previously [*Borovsky and Denton*, 2010a] of ~32 keV/day of heating during high-speed stream-driven storms is plotted as the green dashed diagonal line in the second panel of Figure 8: both types of storms on average exhibit approximately 32 keV/day of heating. This storm time heating of the radiation belt for both types of storms is noted in line 21 of Table 1.

[44] In the bottom panel of Figure 8, the local time average of the superposed average of the omnidirectional 1.1–1.5 MeV electron flux at geosynchronous orbit is plotted. In the day or so before the onset of the storms, the relativistic electron flux of the helmet streamer CIR storms (red) exhibits a temporal decay that follows the number density decay in the top

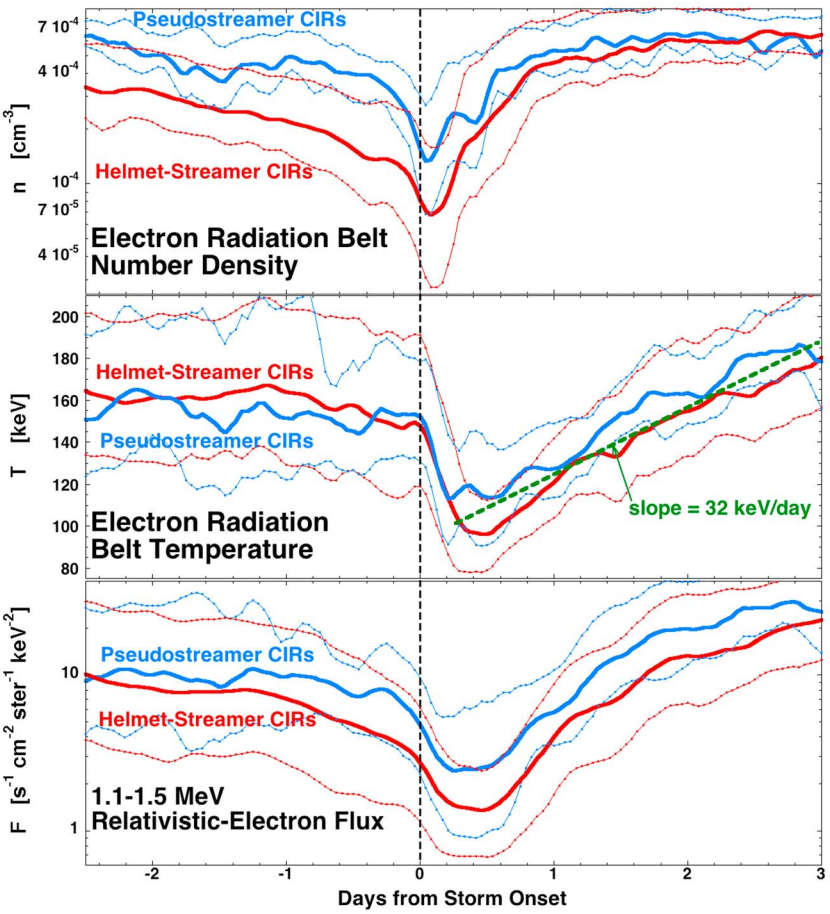

Figure 8. Superposed averages of the properties of the outer electron radiation belt measured at geosynchronous orbit, with the zero epoch being the onset of storm levels of magnetospheric convection. The thick curves are mean values and the thin curves are upper and lower quartiles.

panel of Figure 8. The relativistic electron flux for the pseudostreamer CIR storms (blue) does not as clearly exhibit this pre-storm decay, just as the radiation belt number density does not as clearly exhibit a pre-storm decay for pseudostreamer CIR storms (cf. line 19 of Table 1). Both types of storms exhibit a relativistic electron flux dropout in the early phase of the storm. The onset of the flux dropout (bottom panel) is approximately simultaneous with the onset of the density dropout (top panel). Note however that the duration of the relativistic electron flux dropout (bottom panel) is much greater than the duration of the number density dropout (top panel) and that the number density recovers well before the relativistic electron flux recovers [cf. *Borovsky and Denton*, 2010a, Figure 3]. It has been noted that the flux recovery follows the temporal trend of the radiation belt temperature rather than the trend of the radiation belt density [*Borovsky and Denton*, 2011]. In the days after the storm onset, the 1.1–1.5 MeV omnidirectional electron flux steadily increases for both types of storms (bottom panel): in this time period, the radiation belt temperature steadily increases (second panel) while the number density remains constant (top panel). Hence, the storm time increase in the flux of relativistic electrons appears to be owed to the ~32 keV/day of heating of the radiation belt electrons. This is true for both helmet streamer CIR storms and pseudostreamer CIR storms, as noted in line 22 of Table 1

10. Summary

[45] Superposed epoch analysis was used to study the properties of the solar wind and the magnetosphere during 75 pseudostreamer CIR storms and during 11 helmet streamer CIR storms. The findings of the comparison between pseudostreamer CIR storms and helmet streamer CIR storms are collected in Table 1.

[46] The major differences between storms driven by pseudostreamer CIRs and those driven by helmet streamer CIRs are the following.

[47] 1. Pseudostreamer CIR storms do not tend to have a calm before the storm, whereas helmet streamer CIR storms do. This is a consequence of (a) the Russell-McPherron effect favoring the fast wind for a storm and (b) the presence or absence of a sector reversal ahead of the fast wind.

[48] 2. Pseudostreamer CIR storms tend not to exhibit refilling of the outer plasmasphere before the storm; helmet streamer CIR storms do have refilling before the storm. This is a consequence of the helmet streamer storms having calms before the storms and the pseudostreamer storms not having calms.

[49] 3. Pseudostreamer CIR storms are not as long lived on average as helmet streamer CIR storms, probably owing to the smaller coronal holes associated with pseudostreamers.

[50] 4. Pseudostreamer CIR storms have weaker superdense plasma sheets than do helmet streamer CIR storms. This is a consequence of the solar wind density being higher at the time of storm onset for helmet streamer storms than it is for pseudostreamer storms.

[51] 5. Pseudostreamer CIR storms do not clearly show the pre-storm exponential decay of the radiation belt; helmet streamer CIR storms do show a pre-storm decay. This potential difference could be a consequence of the helmet streamer storms tending to have built-up outer plasmaspheres before the storms and the pseudostreamer storms having an absence of outer plasmaspheres before the storm.

[52] 6. Pseudostreamer CIR storms have weaker radiation belt dropouts than helmet streamer CIR storms. The reason could be a combination of the strength of the solar wind ram pressure and the density of the plasma sheet during the early phases of the storms.

[53] Some similarities between the two types of storms are the following.

[54] 1. Both types of storms have superdense and extra hot plasma sheets.

[55] 2. Both types of storms produce high levels of spacecraft charging.

[56] 3. Both types of storms have enhanced levels of ULF fluctuations.

[57] 4. Both types of storms exhibit radiation belt density recovery and long-duration heating of the electron radiation belt, leading to high fluxes of relativistic electrons.

[58] 5. Both types of storms have similar plasmaspheric drainage plumes, despite the difference in the amount of filling of the outer plasmasphere prior to storm onset.

11. Discussion

[59] Several issues about CIR-driven geomagnetic storms have been raised by the separation of storms into helmet streamer CIR storms and pseudostreamer CIR storms.

[60] One second mystery is why the plasmaspheric drainage plumes of the two types of storms seem similar, whereas the amount of outer plasmaspheric plasma prior to storm onset is very different. For CIR-driven storms, on average, the estimated plasma flow in drainage plumes matches estimates for the amount of outer plasmaspheric plasma [*Borovsky and Denton*, 2008], but comparison of plumes from filled plasmaspheres with plumes from unfilled plasmaspheres have never been compared before this present study.

[61] A second mystery is the reason for the rapid decline of the magnetic field strength enhancement of the dayside magnetosphere in the early phase of the helmet streamer CIR storms (cf. Figure 7). This decrease occurs well before the enhanced ram pressure of the solar wind declines. This rapid decrease in the dayside magnetic field strength has been examined for CIR-driven storms in general [*Borovsky and Denton*, 2010b] and no fully convincing explanation has been found.

[62] A longstanding issue in the physics of CIR-driven storms is the role of solar wind fluctuations in the driving of the magnetosphere during the high-speed streams following the CIRs [*Tsurutani and Gonzalez*, 1987; *Tsurutani et al*., 2006; *Denton et al*., 2008; *Lyons et al*., 2009]. Perhaps solar wind fluctuations are playing important roles in the driving of the magnetosphere during high-speed stream-driven storms; but on the contrary, the G + B driver function (bottom panel of Figure 2), which ignores solar wind fluctuations, does a very good job of predicting the *Kp* index (top panel of Figure 4).

[63] A larger number of categorized storm events are desirable to firm up the conclusions of this report. In particular, it would significantly advance our understanding of storms to have abundant enough statistics to determine how much of the 66% of storms that have calms and the 33% that do not [*Borovsky and Steinberg*, 2006] is owed to the fraction of storms that are helmet streamer CIR storms versus the fraction that are pseudostreamer CIR storms. Gathering a substantial number of additional quality storms will have to wait until the next declining phase of the solar cycle.

[64] **Acknowledgments.** The authors wish to thank John Steinberg for helpful conversations and Tom Cayton, Howard Singer, Ruth Skoug, and Michelle Thomsen for the data. This work was supported at Space Science Institute by the NASA CCMSM-24 Program and the NSF GEM Program, at the University of Michigan by the NASA Geospace SR&T Program, at Los Alamos National Laboratory under the NSF SHINE Program, and at the University of Lancaster by Science and Technology Funding Council grant ST/I000801/1.

[65] Philippa Browning thanks the reviewer for his assistance in evaluating this paper.

References

Antiochos, S. K., Z. Mikic, V. S. Titov, R. Lionello, and J. A. Linker (2011), A model for the sources of the slow solar wind, *Astrophys. J.*, *731*, 112.

Bame, S. J., D. J. McComas, M. F. Thomsen, B. L. Barraclough, R. C. Elphic, J. P. Glore, J. T. Gosling, J. C. Chavez, E. P. Evans, and F. J. Wymer (1993), Magnetospheric plasma analyzer for spacecraft with constrained resources, *Rev. Sci. Instrum.*, *64*, 1026–1033.

Belian, R. D., G. R. Gisler, T. Cayton, and R. Christensen (1992), High-Z energetic particles at geosynchronous orbit during the great solar proton event series of October 1989, *J. Geophys. Res.*, *97*, 16,897–16,906.

Belian, R. D., T. E. Cayton, R. A. Christensen, J. C. Ingraham, M. M. Meier, G. D. Reeves, and A. J. Lazarus (1996), Relativistic electrons in the outer-zone: An 11 year cycle; their relation to the solar wind, in *Workshop on the Earth's Trapped Particle Environment*, edited by G. D. Reeves, pp. 13–18, American Institute of Physics, Woodbury, N.Y.

Borovsky, J. E. (2008), The rudiments of a theory of solar-wind/magnetosphere coupling derived from first principles, *J. Geophys. Res.*, *113*, A08228, doi:10.1029/2007JA012646.

Borovsky, J. E. (2013), Physical improvements to the solar-wind reconnection control function for the Earth's magnetosphere, *J. Geophys. Res. Space Physics*, *118*, 2113–2121, doi:10.1002/jgra.50110.

Borovsky, J. E., and M. H. Denton (2006), The differences between CME-driven storms and CIR-driven storms, *J. Geophys. Res.*, *111*, A07S08, doi:10.1029/2005JA011447.

Borovsky, J. E., and M. H. Denton (2008), A statistical look at plasmaspheric drainage plumes, *J. Geophys. Res.*, *113*, A09221, doi:10.1029/2007JA012994.

Borovsky, J. E., and M. H. Denton (2009a), Relativistic-electron dropouts and recovery: A superposed-epoch study of the magnetosphere and the solar wind, *J. Geophys. Res.*, *114*, A02201, doi:10.1029/2008JA013128.

Borovsky, J. E., and M. H. Denton (2009b), Electron loss rates from the outer electron radiation belt caused by the filling of the outer plasmasphere: The calm before the storm, *J. Geophys. Res.*, *114*, A11203, doi:10.1029/2009JA014063.

Borovsky, J. E., and M. H. Denton (2010a), On the heating of the outer radiation belt to produce high fluxes of relativistic electrons: Measured heating rates for high-speed-stream-driven storms, *J. Geophys. Res.*, *115*, A12206, doi:10.1029/2010JA015342.

Borovsky, J. E., and M. H. Denton (2010b), The magnetic field at geosynchronous orbit during high-speed-stream-driven storms: Connections to the solar wind, the plasma sheet, and the outer electron radiation belt, *J. Geophys. Res.*, *115*, A08217, doi:10.1029/2009JA015116.

Borovsky, J. E., and M. H. Denton (2011), Evolution of the magnetotail energetic-electron population during high-speed-stream-driven storms:

Evidence for the leakage of the outer electron radiation belt into the Earth's magnetotail, *J. Geophys. Res.*, *116*, A12228, doi:10.1029/2011JA016713.

Borovsky, J. E., and J. T. Steinberg (2006), The "calm before the storm" in CIR/magnetosphere interactions: Occurrence statistics, solar-wind statistics, and magnetospheric preconditioning, *J. Geophys. Res.*, *111*, A07S10, doi:10.1029/2005JA011397.

Borovsky, J. E., M. F. Thomsen, and D. J. McComas (1997), The superdense plasma sheet: Plasmaspheric origin, solar-wind origin, or ionospheric origin?, *J. Geophys. Res.*, *102*, 22,089–22,097.

Borovsky, J. E., M. F. Thomsen, and R. C. Elphic (1998a), The driving of the plasma sheet by the solar wind, *J. Geophys. Res.*, *103*, 17,617–17,639.

Borovsky, J. E., M. F. Thomsen, R. C. Elphic, T. E. Cayton, and D. J. McComas (1998b), The transport of plasma sheet material from the distant tail to geosynchronous orbit, *J. Geophys. Res.*, *103*, 20,297–20,331.

Cayton, T. E., and R. D. Belian (2007), Numerical modeling of the synchronous orbit particle analyzer (SOPA, Version 2) that flew on S/C 1990-095, LA Rep. LA-14335, Los Alamos Natl. Lab., Los Alamos, N. M.

Cayton, T. E., R. D. Belian, S. P. Gary, T. A. Fritz, and D. N. Baker (1989), Energetic electron components at geosynchronous orbit, *Geophys. Res. Lett.*, *16*, 147–150.

Crooker, N. U., and R. L. McPherron (2012), Coincidence of composition and speed boundaries of the slow solar wind, *J. Geophys. Res.*, *117*, A09104, doi:10.1029/2012JA017837.

Crooker, N. U., S. W. Kahler, D. E. Larson, and R. P. Lin (2004a), Large-scale magnetic field inversions at sector boundaries, *J. Geophys. Res.*, *109*, A03108, doi:10.1029/2003JA010278.

Crooker, N. U., C.-L. Huang, S. M. Lamassa, D. E. Larson, S. W. Kahler, and H. E. Spence (2004b), Heliospheric plasma sheets, *J. Geophys. Res.*, *109*, A03107, doi:10.1029/2003JA010170.

Crooker, N. U., S. K. Antiochos, X. Zhao, and M. Neugebauer (2012), Global network of slow solar wind, *J. Geophys. Res.*, *117*, A04104, doi:10.1029/2011JA017236.

DeForest, S. E. (1972), Spacecraft charging at synchronous orbit, *J. Geophys. Res.*, *77*, 651–659.

Denton, M. H., and J. E. Borovsky (2008), Superposed epoch analysis of high-speed-stream effects at geosynchronous orbit: Hot plasma, cold plasma, and the solar wind, *J. Geophys. Res.*, *113*, A07216, doi:10.1029/2007JA012998.

Denton, M. H., and J. E. Borovsky (2009), The superdense plasma sheet in the magnetosphere during high-speed-steam-driven storms: Plasma transport timescales, *J. Atmos. Sol. Terr. Phys.*, *71*, 1045.

Denton, M. H., and J. E. Borovsky (2012), Magnetosphere response to high-speed solar wind streams: A comparison of weak and strong driving and the importance of extended periods of fast solar wind, *J. Geophys. Res.*, *117*, A00L05, doi:10.1029/2011JA017124.

Denton, M. H., M. F. Thomsen, H. Korth, S. Lynch, J. C. Zhang, and M. W. Liemohn (2005), Bulk plasma properties at geosynchronous orbit, *J. Geophys. Res.*, *110*, A07223, doi:10.1029/2004JA010861.

Denton, M. H., J. E. Borovsky, R. M. Skoug, M. F. Thomsen, B. Lavraud, M. G. Henderson, R. L. McPherron, J. C. Zhang, and M. W. Liemohn (2006), Geomagnetic storms driven by ICME- and CIR-dominated solar wind, *J. Geophys. Res.*, *111*, A07S07, doi:10.1029/2005JA011436.

Denton, M. H., J. E. Borovsky, R. B. Horne, R. L. McPherron, S. K. Morley, and B. T. Tsurutani (2008), High-speed solar wind streams: A call for key research, *Eos Trans. Am. Geophys. Soc.*, *89*, 62.

Denton, M. H., J. E. Borovsky, and T. E. Cayton (2010), A density-temperature description of the outer electron radiation belt during geomagnetic storms, *J. Geophys. Res.*, *115*, A01208, doi:10.1029/2009JA014183.

Dunham, W. D., S. A. MacIntyre, and C. R. Upton (1996), Design and performance of the GOES-8 high resolution magnetometer, *SPIE Proc.*, *2812*, 365.

Elliott, H. A., D. J. McComas, N. A. Schwadron, J. T. Gosling, R. M. Skoug, G. Gloeckler, and T. H. Zurbuchen (2005), An improved expected temperature formula for identifying ICMEs, *J. Geophys. Res.*, *110*, A04103, doi:10.1029/2004JA010794.

Elphic, R. C., M. F. Thomsen, J. E. Borovsky, and D. J. McComas (1999), Inner edge of the electron plasma sheet: Empirical models of boundary location, *J. Geophys. Res.*, *104*, 22,679–22,693.

Foullon, C., et al (2011), Plasmoid releases in the heliospheric current sheet and associated coronal hole boundary layer evolution, *Astrophys. J.*, *737*(1), 16, doi:10.1088/0004-637X/737/1/16.

Gloeckler, G., et al (1998), Investigation of the composition of solar and interstellar matter using solar wind and pickup ion measurements with SWICS and SWIMS on the ACE spacecraft, *Space Sci. Rev.*, *86*, 497–539.

Gosling, J. T., V. Pizzo, and S. J. Bame (1973), Anomalously low proton temperatures in the solar wind following interplanetary shock waves – Evidence for magnetic bottles, *J. Geophys. Res.*, *78*, 2001–2009.

Gosling, J. T., D. N. Baker, S. J. Bame, W. C. Feldman, R. D. Zwickl, and E. J. Smith (1987), Bidirectional solar wind electron heat flux events, *J. Geophys. Res.*, *92*, 8519–8535.

Gussenhoven, M. S., D. A. Hardy, and N. Heinemann (1983), Systematics of the equatorward diffuse auroral boundary, *J. Geophys. Res.*, *88*, 5692–5708.

King, J. H., and N. E. Papitashvili (2005), Solar wind spatial scales in and comparisons of hourly Wind and ACE plasma and magnetic field data, *J. Geophys. Res.*, *110*, A02104, doi:10.1029/2004JA010649.

Kissinger, J., R. L. McPherron, T.-S. Hsu, and V. Angelopoulos (2011), Steady magnetospheric convection and stream interfaces: Relationship over a solar cycle, *J. Geophys. Res.*, *116*, A00I19, doi:10.1029/2010JA015763.

Lavraud, B., and J. E. Borovsky (2008), Altered solar wind-magnetosphere interaction at low Mach numbers: Coronal mass ejections, *J. Geophys. Res.*, *113*, A00B08, doi:10.1029/2008JA013192.

Liu, Y. (2007), Halo coronal mass ejections and configuration of the ambient magnetic fields, *Astrophys. J.*, *654*, L171–L174.

Lyons, L. R., D.-Y. Lee, H.-J. Kim, J. A. Hwang, R. M. Thorne, R. B. Horne, and A. J. Smith (2009), Solar-wind-magnetosphere coupling, including relativistic electron energization, during high-speed streams, *J. Atmos. Sol. Terr. Phys.*, *71*, 1059–1072.

McComas, D. J., S. J. Blame, P. Barker, W. C. Feldman, J. L. Phillips, P. Riley, and J. W. Griffee (1998), Solar Wind Electron Proton Alpha Monitor (SWEPAM) for the Advanced Composition Explorer, *Space Sci. Rev.*, *86*, 563–612.

McPherron, R. L., D. N. Baker, and N. U. Crooker (2009), Role of the Russell-McPherron effect in the acceleration of relativistic electrons, *J. Atmos. Sol. Terr. Phys.*, *71*, 1032–1044.

Neugebauer, M., P. C. Liewer, B. E. Goldstein, X. Zhou, and J. T. Steinberg (2004), Solar wind stream interaction regions without sector boundaries, *J. Geophys. Res.*, *109*, A10102, doi:10.1029/2004JA010456.

Newell, P. T., T. Sotirelis, K. Liou, C.-I. Meng, and F. J. Rich (2007), A nearly universal solar wind-magnetosphere coupling function inferred from 10 magnetospheric state variables, *J. Geophys. Res.*, *112*, A01206, doi:10.1029/2006JA012015.

Pneuman, G. W. (1968), Some general properties of helmeted coronal structures, *Sol. Phys.*, *3*, 578–597.

Richardson, I. G., and H. V. Cane (1995), Regions of abnormally low proton temperature in the solar wind (1965–1991) and their association with ejecta, *J. Geophys. Res.*, *100*, 23,397–23,412.

Richardson, I. G., G. Wibberenz, and H. V. Cane (1996), The relationship between recurring cosmic ray depressions and corotating solar wind streams at 1 AU: IMP 8 and Helios 1 and 2 anticoincidence guard rate observations, *J. Geophys. Res.*, *101*, 13,483–13,496.

Riley, P., and J. G. Luhmann (2012), Interplanetary signatures of unipolar streamers and the origin of the slow solar wind, *Sol. Phys.*, *277*, 355–373.

Rusin, V., M. Druckmuller, P. Aniol, M. Minarovjech, M. Saniga, Z. Mikic, J. A. Linker, R. Lionello, P. Riley, and V. S. Titov (2010), Comparing eclipse observations of the 2008 August 1 solar coronal with an MHD model prediction, *Astron. Astrophys.*, *513*, A45, doi:10.1051/0004-6361/200912778.

Russell, C. T., and R. L. McPherron (1973), Semiannual variation of geomagnetic activity, *J. Geophys. Res.*, *78*, 92.

Singer, H. J., L. Matheson, R. Grubb, A. Newman, and S. D. Bouwer (1996), Monitoring space weather with the GOES magnetometers, *SPIE Proc.*, *2812*, 299–308.

Siscoe, G., and D. Intriligator (1993), Three views of two giant streams: Aligned observations at 1 AU, 4.6 AU, and 5.9 AU, *Geophys. Res. Lett.*, *20*, 2267–2270.

Skoug, R. M., W. C. Feldman, J. T. Gosling, D. J. McComas, and C. W. Smith (2000), Solar wind electron characteristics inside and outside coronal mass ejections, *J. Geophys. Res.*, *105*, 23,069–23,084.

Smith, C. W., M. H. Acuna, L. F. Burlaga, J. L'Heureux, N. F. Ness, and J. Scheifele (1998), The ACE Magnetic Fields Experiment, *Space Sci. Rev.*, *86*, 613–632.

Spreiter, J. R., and S. S. Stahara (1994), Gasdynamic and magnetohydrodynamic modeling of the magnetosheath: A tutorial, *Adv. Space Sci.*, *14*(7), 5–9.

Thomsen, M. F. (2004), Why *Kp* is such a good measure of magnetospheric convection, *Space Weather*, *2*, S11044, doi:10.1029/2004SW000089.

Thomsen, M. F., D. J. McComas, J. E. Borovsky, and R. C. Elphic (1998), The magnetospheric trough, in *Geospace Mass Transport and Energy Flow: Results from the International Solar-Terrestrial Physics Program*, edited by J. L. Horwitz et al., pp. 355–369, AGU, Washington, D. C.

Thomsen, M. F., E. Noveroske, J. E. Borovsky, and D. J. McComas (1999), Calculating the moments from measurements by the Los Alamos magnetospheric plasma analyzer, LA-13566-MS, Los Alamos National Laboratory.

Titov, V. S., Z. Mikic, J. A. Linker, R. Lionello, and S. K. Antiochos (2011), Magnetic topology of coronal hole linkages, *Astrophys. J.*, *731*, 111.

Tsurutani, B. T., and W. D. Gonzalez (1987), The cause of high-intensity long-duration continuous AE Activity (HILDCAAS): Interplanetary Alfven wave trains, *Planet. Space Sci.*, *35*, 405–412.

Tsurutani, B. T., A. J. Mannucci, B. A. Iijima, A. Komjathy, A. Saiton, T. Tsuda, O. P. Verkhoglyadova, W. D. Gonzalez, and F. L. Guarnieri (2006), Dayside ionospheric (GPS) response to corotating solar wind streams, in *Recurrent Magnetic Storms: Corotating Solar Wind Streams*, Geophys. Monog. 167, vol. 175, pp. 245, AGU, Washington, D.C.

Tsyganenko, N. A., H. J. Singer, and J. C. Kasper (2003), Storm-time distortion of the inner magnetosphere: How severe can it get?, *J. Geophys. Res.*, *108*, 1209, doi:10.1029/2002JA009808.

Wang, Y.-M., N. R. Sheeley, D. G. Socker, R. A. Howard, and N. B. Rich (2000), The dynamical nature of coronal streamers, *J. Geophys. Res.*, *105*, 25,133–25,142.

Wang, Y.-Y., J. B. Biersteker, N. R. Sheeley, S. Koutchmy, J. Mouette, and M. Druckmuller (2007), The solar eclipse of 2006 and the origin of raylike features in the white-light corona, *Astrophys. J.*, *660*, 882–892.

Wang, Y.-M., R. Grappin, E. Robbecht, and N. R. Sheeley (2012), On the nature of the solar wind from coronal pseudostreamers, *Astrophys. J.*, *749*, 182.

Winterhalter, D., E. J. Smith, M. E. Burton, N. Murphy, and D. J. McComas (1994), The heliospheric plasma sheet, *J. Geophys. Res.*, *99*, 6667–6680.

Zhao, L., T. H. Zurbuchen, and L. A. Fisk (2009), Global distribution of the solar wind during solar cycle 23: ACE observations, *Geophys. Res. Lett.*, *36*, L14104, doi:10.1029/2009GL039181.